

# Hybrid Analytical Modeling of Saturated Linear and Rotary Electrical Machines: Integration of Fourier Modeling and Magnetic Equivalent Circuits

J. Bao<sup>1</sup>, B. L. J. Gysen<sup>1</sup>, and E. A. Lomonova

Department of Electrical Engineering, Eindhoven University of Technology, 5612 AP Eindhoven, The Netherlands

This paper presents a 2-D hybrid analytical modeling method for the analysis of the magnetostatic field distribution with the capability of including nonlinear materials. The model combines Fourier modeling, which is accurate and fast, with meshed magnetic equivalent circuits that have unique permeability in mesh elements and, therefore, can model local saturation. To present the diverse applicability of the proposed method, it is applied to a linear machine with permanent magnet excitation and a rotary machine with current excitation. Magnetic field calculations are compared with finite-element analysis (FEA) with good agreement.

**Index Terms**—Analytical modeling, electrical machine, Fourier analysis, hybrid modeling, magnetic equivalent circuit (MEC), saturation.

## I. INTRODUCTION

**M**ODELING of the electromagnetic field distribution is of major importance in the design process of electromagnetic devices. In recent years, several advanced methods are being researched, e.g., Schwarz–Christoffel (SC) method, boundary element (BE) method, and Fourier modeling [1]. The SC mapping provides an analysis tool that allows the transformation from polygonal boundaries to a simpler domain, circumventing difficulties encountered when solving boundary value problems on complicated geometries [2], [3]. Facing the challenge associated with mapping function evaluation, it is developed to use the SC toolbox in MATLAB to automate mapping numerically [2]. It is successfully applied in [4] for a switched reluctance machine (SRM) with linear materials. The BE method is derived from the Poisson or Laplace equations in integral form. The integral equation only has to be evaluated at the boundaries of the domain, so that the number of elements can be reduced significantly compared with the finite-element method [3]. However, the requirement of linear material property limits the application of the method for structures involving soft-magnetic material [5].

For structures with periodicity, Fourier modeling is particularly interesting; however, the limitation is the unavailability to take circumferential variations of material property (e.g., magnetic permeability) into account [1], which is a significant drawback in the case of stator/rotor slotting [6], [7]. In [7]–[11], a hybrid analytical modeling (HAM) technique that integrates the Fourier modeling and meshed magnetic equivalent circuit (MEC) is discussed. This method is capable of including small geometric features with high-permeable materials. In [8]–[11], the mesh-based MEC is only connected to one side of the Fourier modeling. A promising result of the magnetic field is provided in the air gap in [8] for a linear

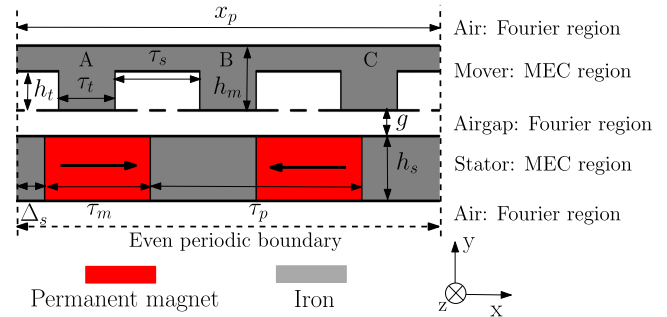


Fig. 1. Geometry of the PM machine in the Cartesian coordinate system.

permanent magnet (PM) structure and cogging force/torque is precisely estimated in [9] for various electromagnetic structures. Furthermore, material nonlinearity is shortly discussed in [10], that calculates the cogging force for PM machines with different slot geometries, considering saturation in the stator. However, the derivation of the MEC formulation regarding the saturation, especially the change in source terms, is not explained. In [7], bidirectional coupling on both sides of the MEC regions are applied, achieving excellent matching of flux density in the overall structure with linear material properties.

In this paper, the incorporation of saturation with the bidirectional-coupled HAM, is further investigated and validated by utilizing locally linearized  $B$ – $H$  relationship for both linear and rotary machines, which are shown in Figs. 1 and 2. The content is first focused on the model formulation and description of magnetic sources (PM/current), followed by the formulation of material nonlinearity in the MEC element and the iterative algorithm. Validation of the proposed method is performed by the comparison with finite-element analysis (FEA).

## II. MODELING FORMULATION

To obtain the magnetic field solution, the following assumptions are made: 1) the problem is described in a 2-D coordinate system; 2) source terms (PM/current) are invariant in the  $z$ -direction; and 3) the problem is quasi-static.

Manuscript received March 16, 2018; revised April 20, 2018; accepted May 9, 2018. Corresponding author: J. Bao (e-mail: j.bao@tue.nl).

Color versions of one or more of the figures in this paper are available online at <http://ieeexplore.ieee.org>.

Digital Object Identifier 10.1109/TMAG.2018.2837896

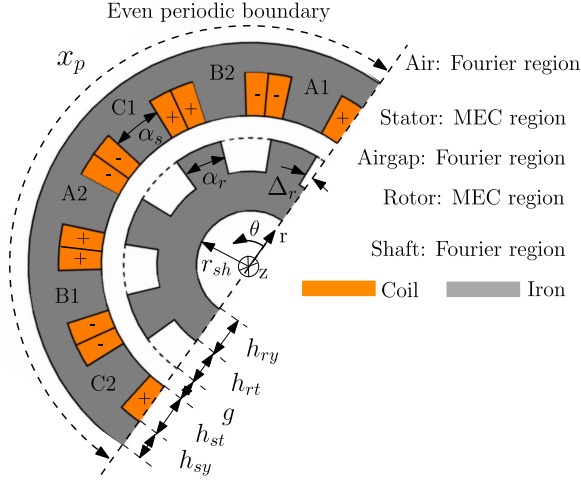


Fig. 2. Geometry of the 12/8 SRM in the polar coordinate system.

TABLE I

DIMENSIONS OF THE MODEL IN CARTESIAN COORDINATE SYSTEM

Parameter	Description	value
$h_m$	Height of mover	5 mm
$g$	Airgap length	0.5 mm
$h_t$	Height of teeth	3 mm
$h_s$	Height of stator	5 mm
$\tau_m$	Magnet width	15 mm
$\tau_p$	Pole pitch	30 mm
$\Delta_s$	Stator position	4 mm
$\tau_t$	Teeth width	8 mm
$\tau_s$	Slot width	12 mm
$x_p$	Width of periodicity	60 mm
$L_z$	Stack length	50 mm

TABLE II

DIMENSIONS OF THE MODEL IN POLAR COORDINATE SYSTEM

Parameter	Description	value
$r_{sh}$	Shaft radius	20.5 mm
$h_{ry}$	Rotor yoke height	10.5 mm
$h_{rt}$	Rotor teeth height	14.5 mm
$g$	Airgap length	0.5 mm
$h_{st}$	Stator teeth height	14.5 mm
$h_{sy}$	Stator yoke height	9.5 mm
$\alpha_s$	Stator tooth arc	16°
$\alpha_r$	Rotor tooth arc	22°
$\Delta_r$	Rotor position	4°
$x_p$	Width of periodicity	180°
$L_z$	Axial length	87.5 mm

To present the diverse applicability of the proposed method for saturated electrical machines, it is applied to two geometries in two coordinate systems with different presences of magnetic sources (PM/current). For the Cartesian coordinate system, a slotted linear PM machine shown in Fig. 1 is modeled, and for the polar coordinate system, a three-phase 12/8 SRM [12] shown in Fig. 2 is modeled. The dimensions are given in Tables I and II, respectively.

In the two examples, periodicities are, respectively, applied in the  $x$ - or  $\theta$ -directions, while regions are divided in the  $y$ - or  $r$ -directions. The division in the regions is shown in Figs. 1 and 2. In general, only the air and shaft regions are modeled using Fourier expressions, since the Fourier modeling divides the geometry in periodical regions with homogeneous permeability and does not allow to model local saturation.

TABLE III

FOURIER FUNCTIONS IN CARTESIAN AND POLAR COORDINATE SYSTEMS

	Cartesian	polar
$B_{psn}$	$a_n e^{\omega_n y} + b_n e^{-\omega_n y}$	$a_n r^{\omega_n - 1} + b_n r^{-\omega_n - 1}$
$B_{pcn}$	$-c_n e^{\omega_n y} - d_n e^{-\omega_n y}$	$-c_n r^{\omega_n - 1} - d_n r^{-\omega_n - 1}$
$B_{qsn}$	$c_n e^{\omega_n y} - d_n e^{-\omega_n y}$	$c_n r^{\omega_n - 1} - d_n r^{-\omega_n - 1}$
$B_{qcn}$	$a_n e^{\omega_n y} - b_n e^{-\omega_n y}$	$a_n r^{\omega_n - 1} - b_n r^{-\omega_n - 1}$

Notes: spatial frequency  $\omega_n = 2\pi n/x_p$ .

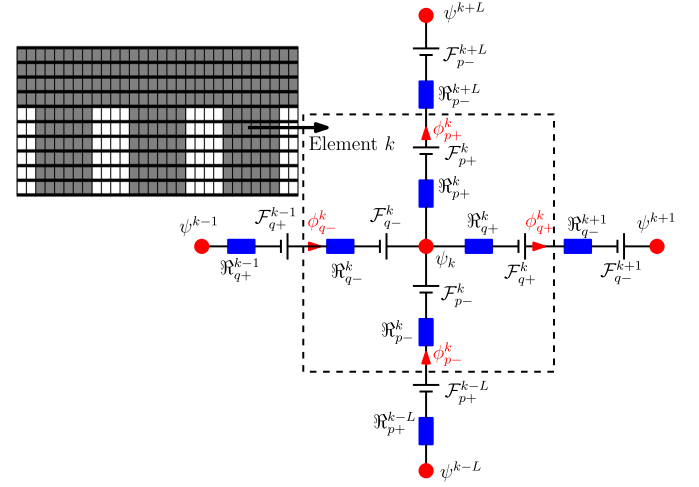


Fig. 3. Schematic graphs of a meshed MEC region and the mesh elements.

The meshed MEC, on the other hand, is used for regions with nonlinear material (such as stator and mover/rotor), since each mesh element is able to have its unique permeability and, hence, is capable to take local saturation into account. For generality of the explanations in the following content, the normal direction ( $y$  or  $r$ ) is referred as the  $p$ -direction, while the tangential direction ( $x$  or  $\theta$ ) is referred as the  $q$ -direction.

#### A. Definition of Fourier Regions

In Fourier regions, the magnetostatic problem is formulated in the terms of magnetic vector potential. Since there are no source terms in Fourier regions, the magnetostatic Maxwell equation reduces to a Laplace equation. The resulting solution of the flux density can be written as

$$\vec{B} = B_p \vec{p} + B_q \vec{q} = \sum_{n=1}^{\infty} (B_{psn} \sin(\omega_n q) + B_{pcn} \cos(\omega_n q)) \vec{p} + \sum_{n=1}^{\infty} (B_{qsn} \sin(\omega_n q) + B_{qcn} \cos(\omega_n q)) \vec{q} \quad (1)$$

where  $B_{psn}$ ,  $B_{pcn}$ ,  $B_{qsn}$ , and  $B_{qcn}$  are listed in Table III [6].

#### B. Definition of MEC Regions

An MEC region is divided into elements with rectangular and circular sector shapes in Cartesian and polar coordinate systems, respectively. Each element contains the information of reluctance, permeability and magnetic source. An example of a meshed MEC region is shown in Fig. 3; as can be seen, the mesh is formed such that the material boundaries

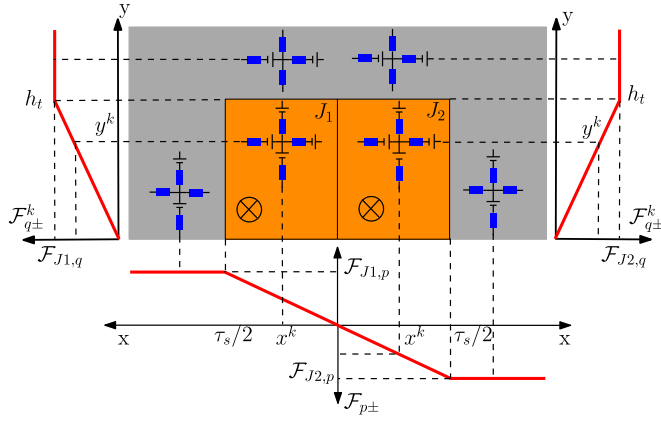


Fig. 4. Current related  $mmf$  for Cartesian coordinate system in the yoke, tooth, and slot, where  $\mathcal{F}_{J1,p} = J_1 A_s l_y^k / (4h_t)$ ,  $\mathcal{F}_{J1,q} = J_1 A_s l_x^k / (2\tau_s)$ ,  $\mathcal{F}_{J2,p} = J_2 A_s l_y^k / (4h_t)$ , and  $\mathcal{F}_{J2,q} = J_2 A_s l_x^k / (2\tau_s)$  with  $A_s = \tau_s h_t / 2$ .

coincide with the mesh element edges and, hence, each MEC element contains homogeneous permeability [7]. In both  $\pm p$ - and  $\pm q$ -directions, a reluctance is assumed as shown in Fig. 3.

Magnetostatic problem in the MEC regions are described using scalar potential. Each MEC element has a potential node, and the flux goes into the node equals to the flux goes out, such conservation of flux gives [7]

$$\phi_{q-}^k + \phi_{p-}^k - \phi_{p+}^k - \phi_{q+}^k = 0. \quad (2)$$

The fluxes in (2) are defined by the potential of element  $k$  and its surroundings, e.g.,

$$\phi_{p-}^k = \frac{\psi^{k-L} - \psi^k + \mathcal{F}_{p+}^{k-L} + \mathcal{F}_{p-}^k}{\mathfrak{N}_{p+}^{k-L} + \mathfrak{N}_{p-}^k} \quad (3)$$

where  $\psi^{k-L}$  represents the potential of element  $k-L$  that is at the bottom of element  $k$ , while  $\mathcal{F}_{p-}^k$ ,  $\mathcal{F}_{p+}^{k-L}$ ,  $R_{p-}^k$ , and  $R_{p+}^{k-L}$  represent the magnetomotive force ( $mmf$ ) and reluctances in  $p$ -directions for element  $k$  and  $k-L$ , respectively.

For elements that represent a PM, the definition of the  $mmf$  is determined by the magnetization and the element size

$$\mathcal{F}_{p+}^k = \mathcal{F}_{p-}^k = \vec{M}_p^k l_p^k / (2\mu_r^k) \quad (4)$$

$$\mathcal{F}_{q+}^k = \mathcal{F}_{q-}^k = \vec{M}_q^k l_q^k / (2\mu_r^k) \quad (5)$$

where  $\vec{M}_p$ ,  $\vec{M}_q$ ,  $l_p^k$ , and  $l_q^k$  are the magnetization and dimensions of element  $k$  in the  $p$ - and  $q$ -directions. For elements related to current excitation, the distribution of the  $mmf$  sources has to fulfill the Ampere's law for any arbitrary paths. In [8], the current is expressed merely in the  $q$ -direction for the situation of homogeneous current density in one slot, while in this paper,  $mmf$  sources are modeled in both  $p$ - and  $q$ -directions for two current densities in one slot. The expressions of current related  $mmf$  are divided into three categories depending on the location, i.e., in the yoke, tooth, or slot. The  $mmf$  in the yoke or tooth only has the values in the  $q$ - or  $p$ -direction, respectively, while both terms are assumed in the slot. The magnitude of these  $mmf$  sources in the Cartesian coordinate system is shown in Fig. 4 and Table IV, that is basically linear to the  $x$  or  $y$  locations of the element ( $x^k$  or  $y^k$ )

TABLE IV  
DISTRIBUTION OF CURRENT-RELATED  $mmf$  IN THE CARTESIAN COORDINATE SYSTEM

Pos.	$\mathcal{F}_{p\pm}^k$ for $J_1$	$\mathcal{F}_{q\pm}^k$ for $J_1$	$\mathcal{F}_{p\pm}^k$ for $J_2$	$\mathcal{F}_{q\pm}^k$ for $J_2$
Yoke	0	$\mathcal{F}_{J1,q}^k$	0	$\mathcal{F}_{J2,q}^k$
Tooth	$\mathcal{F}_{J1,p}^k$	0	$-\mathcal{F}_{J2,p}^k$	0
Slot	$2x^k \mathcal{F}_{J1,p} / \tau_s$	$y^k \mathcal{F}_{J1,q} / h_t$	$-2x^k \mathcal{F}_{J2,p} / \tau_s$	$y^k \mathcal{F}_{J2,q} / h_t$

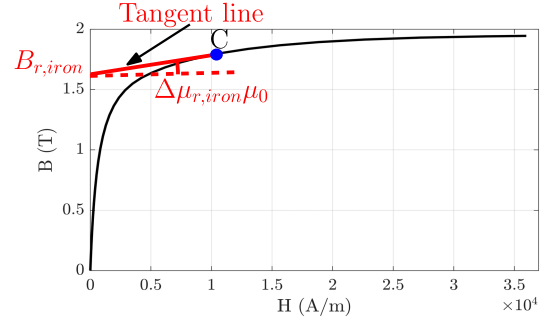


Fig. 5.  $B$ - $H$  curve of the iron used in the examples and the flowchart of the HAM.

before reaching the coil edges. The derivation in the polar coordinate system is similar and, hence, not repeated here.

### C. Boundary Conditions

After obtaining the expressions of the magnetic field inside the MEC and Fourier regions, the boundary conditions are defined. Between the Fourier and MEC regions, the continuity of magnetic field has to be ensured, i.e., the consistent normal flux density and the tangential magnetic field intensity in both the spatial frequency and the space domains. The explanations are elaborated in [7]. At the edge of the outer air and shaft regions, the magnetic field vanishes to zero; the implementation is described in [7] and [13].

## III. MODELING OF NONLINEAR MATERIAL

The  $B$ - $H$  characteristic of the soft magnetic material used in this paper is shown in Fig. 5. For a random working point  $C$ , the expression of  $B$ - $H$  relationship can be locally linearized by a tangent line and the expression becomes

$$H_C = \frac{B_C}{\mu_0 \Delta \mu_{r,iron}} - \frac{1}{\Delta \mu_{r,iron}} \frac{B_{r,iron}}{\mu_0} \quad (6)$$

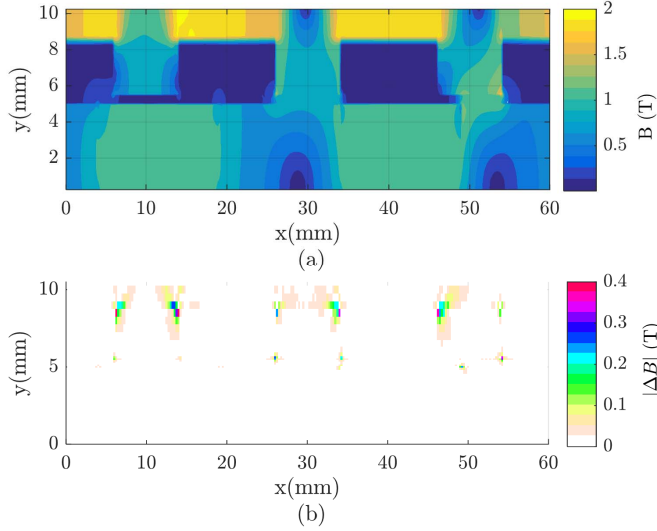


Fig. 6. Magnetic flux density for the PM machine. (a) Magnitude of flux density obtained by HAM. (b) Difference between FEA and HAM.

where  $\Delta\mu_{r,iron}$  is the incremental relative permeability defined by the slope of the tangent line and  $B_{r,iron}$  is the remnant magnetic flux density defined by the intercept. By such expression, it is possible to make an analogy of the term “ $B_{r,iron}/\mu_0$ ” to the magnetization of a PM. Since the magnitude of  $B_{r,iron}$  is positively correlated with the flux density, the “magnetization” is decomposed in  $pq$ -axes using the following expressions:

$$\vec{M}_{p,iron} = \frac{B_p}{\sqrt{B_p^2 + B_q^2}} \frac{B_{r,iron}}{\mu_0} \vec{p} \quad (7)$$

$$\vec{M}_{q,iron} = \frac{B_q}{\sqrt{B_p^2 + B_q^2}} \frac{B_{r,iron}}{\mu_0} \vec{q} \quad (8)$$

which defines a Pythagorean theorem between flux density in  $pq$ -axes ( $B_p$  and  $B_q$ ) and the “magnetization.” As such, the material property of iron is defined by  $\Delta\mu_{r,iron}$  and additional  $mmf$  sources obtained by (4)–(8).

The saturation problem is solved iteratively using the flow-chart shown in Fig. 5. For each iterative step, the reluctances and  $mmf$  have to be re-calculated using the updated  $\Delta\mu_{r,iron}$ ,  $\vec{M}_{p,iron}$ , and  $\vec{M}_{q,iron}$ . Values of  $B_p$  and  $B_q$  are derived by solving the boundary conditions with the newly defined MEC. Afterward,  $\Delta\mu_{r,iron}$ ,  $\vec{M}_{p,iron}$ , and  $\vec{M}_{q,iron}$  are updated corresponding to the newly obtained  $B_p$  and  $B_q$  [14]. Different convergence conditions are applicable, e.g., the difference of force or torque between two adjacent iterative steps is smaller than a certain level (0.2% in this paper).

#### IV. FINITE-ELEMENT VERIFICATION

The modeling method is validated by the FEA. For PM machine, the magnitude of the flux density obtained by the HAM and the difference compared with FEA is shown in Fig. 6. For the SRM example, the comparison of the flux density between the HAM and the FEA in the center of the air gap is shown in Fig. 7. The flux linkage waveforms for both

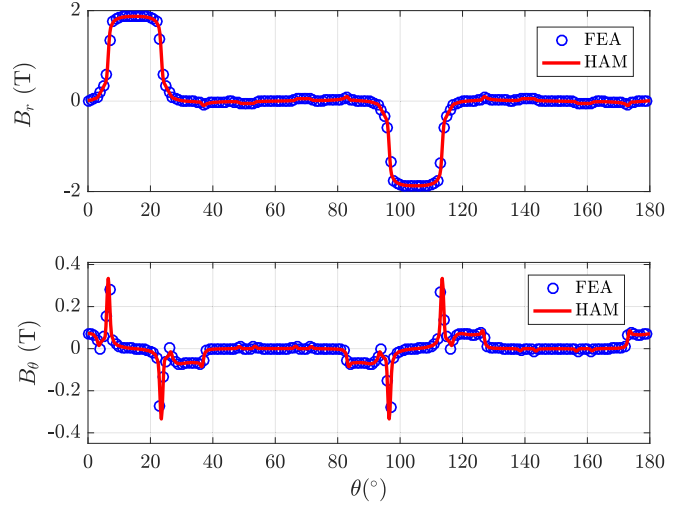


Fig. 7. Magnetic flux density obtained by FEA and HAM in the center of the air gap for the SRM (current density 16 A/mm<sup>2</sup> in phase A). (a) Radial component. (b) Circumferential component.

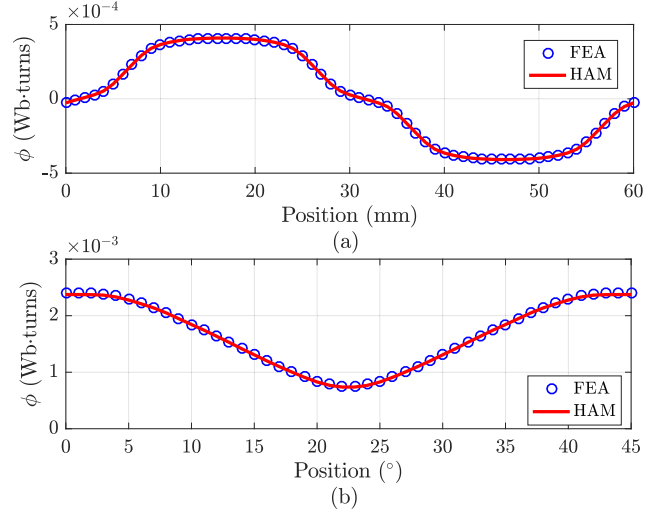


Fig. 8. Flux linkage waveforms of (a) phase A in PM machine at no load and (b) coil A<sub>1</sub> in SRM for current density = 16 A/mm<sup>2</sup> in phase A.

machines are shown in Fig. 8. An overall excellent agreement is observed, showing that the algorithm for saturation is valid.

#### V. CONCLUSION

This paper uses the HAM that integrates meshed MEC and Fourier modeling to calculate the magnetic field in saturated electrical machines. It shows the capability to obtain accurate results in both Cartesian and polar coordinate systems with the PM or current excitations. This method has the potential to be faster than FEA, since the air-gap region is not meshed, while a high mesh density is required in FEA. In addition, since the expression of the magnetic field in the air gap is obtained analytically, force/torque calculations are straightforward and fast, since the Maxwell stress tensor can be solved analytically. Furthermore, the HAM implemented in MATLAB can easily be integrated with algorithms for topology and geometry optimization. Future research will focus on implementation for different motor topologies and derivation of secondary parameters.

## ACKNOWLEDGEMENT

This work was supported in part by the Eindhoven University of Technology, in part by Prodrive Technologies, and in part by Punch Powertrain.

## REFERENCES

- [1] R. L. J. Sprangers, J. J. H. Paulides, B. L. J. Gysen, and E. A. Lomonova, "Magnetic saturation in semi-analytical harmonic modeling for electric machine analysis," *IEEE Trans. Magn.*, vol. 52, no. 2, pp. 1–10, Feb. 2016.
- [2] T. C. O'Connell and P. T. Krein, "The Schwarz–Christoffel analytical method applied to electric machine slot shape optimization," in *Proc. IEEE Int. Elect. Mach. Drives Conf.*, May 2007, pp. 341–346.
- [3] D. C. J. Krop, "Integration of dual electromagnetic energy conversions: Linear actuation with integrated contactless energy transfer," Ph.D. dissertation, Dept. Elect. Eng., Eindhoven Univ. Technol., Eindhoven, The Netherlands, 2013, pp. 47–74.
- [4] L. Gu, E. Bostanci, M. Moallem, S. Wang, and P. Devendra, "Analytical calculation of the electromagnetic field in SRM using conformal mapping method," in *Proc. IEEE Transp. Electrification Conf. Expo. (ITEC)*, Jun. 2016, pp. 1–6.
- [5] J. R. M. van Dam, J. J. H. Paulides, W. S. P. Robertson, M. Dhaens, and E. A. Lomonova, "Analytical surface charge method for rotated permanent magnets: Boundary element method comparison and experimental validation," *IEEE Trans. Magn.*, vol. 52, no. 7, pp. 1–4, Jul. 2016.
- [6] B. L. J. Gysen, K. J. Meessen, J. J. H. Paulides, and E. A. Lomonova, "General formulation of the electromagnetic field distribution in machines and devices using Fourier analysis," *IEEE Trans. Magn.*, vol. 46, no. 1, pp. 39–52, Jan. 2010.
- [7] K. J. W. Pluk, J. W. Jansen, and E. A. Lomonova, "Hybrid analytical modeling: Fourier modeling combined with mesh-based magnetic equivalent circuits," *IEEE Trans. Magn.*, vol. 51, no. 8, pp. 1–10, Aug. 2015.
- [8] S. Ouagued, Y. Amara, and G. Barakat, "Comparison of hybrid analytical modelling and reluctance network modelling for pre-design purposes," *Math. Comput. Simul.*, vol. 130, pp. 3–21, Dec. 2016.
- [9] S. Ouagued, A. A. Diriye, Y. Amara, and G. Barakat, "A general framework based on a hybrid analytical model for the analysis and design of permanent magnet machines," *IEEE Trans. Magn.*, vol. 51, no. 11, pp. 1–4, Dec. 2015.
- [10] S. Ouagued, Y. Amara, and G. Barakat, "Cogging force analysis of linear permanent magnet machines using a hybrid analytical model," *IEEE Trans. Magn.*, vol. 52, no. 7, pp. 1–4, Jul. 2016.
- [11] Y. Laoubi, M. Dhifli, G. Verez, Y. Amara, and G. Barakat, "Open circuit performance analysis of a permanent magnet linear machine using a new hybrid analytical model," *IEEE Trans. Magn.*, vol. 51, no. 3, pp. 1–4, Mar. 2015.
- [12] W. Ding, L. Liu, J. Lou, and Y. Liu, "Comparative studies on mutually coupled dual-channel switched reluctance machines with different winding connections," *IEEE Trans. Magn.*, vol. 49, no. 11, pp. 5574–5589, Nov. 2013.
- [13] B. L. J. Gysen, E. Ilhan, K. J. Meessen, J. J. H. Paulides, and E. A. Lomonova, "Modeling of flux switching permanent magnet machines with Fourier analysis," *IEEE Trans. Magn.*, vol. 46, no. 6, pp. 1499–1502, Jun. 2010.
- [14] A. Daghigh, H. Javadi, and A. Javadi, "Improved analytical modeling of permanent magnet leakage flux in design of the coreless axial flux permanent magnet Generator," *Can. J. Elect. Comput. Eng.*, vol. 40, no. 1, pp. 3–11, 2017.